Physics of Fluids

RESEARCH ARTICLE | APRIL 15 2024

Coexistence of passive vortex-induced vibrations and active pitch oscillation triggered by a square cylinder attached with a deformable splitter plate

Aravindhan Venkatesh; Jiqiang Niu (牛纪强) ; Xiao Xue (薛骁) ; Zheng-Wei Chen (陈争卫) ;
Hua-Dong Yao (姚华栋) ✉

Physics of Fluids 36, 043612 (2024)
https://doi.org/10.1063/5.0200566

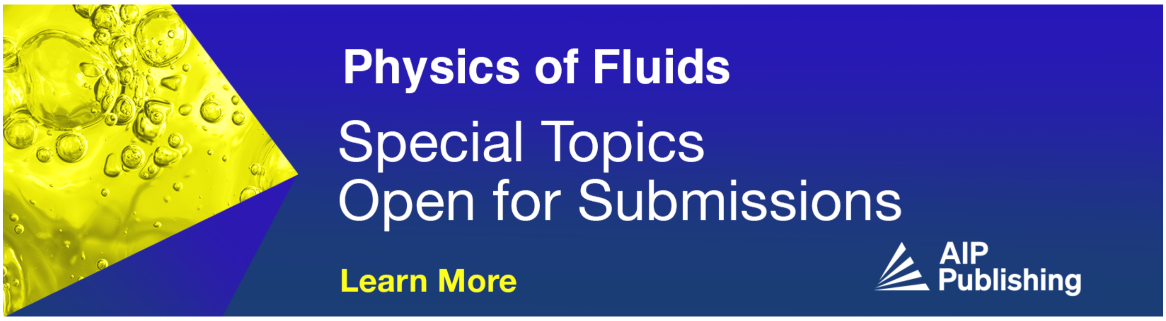

AIP Publishing

Physics of Fluids ARTICLE pubs.aip.org/aip/pof

Coexistence of passive vortex-induced vibrations and active pitch oscillation triggered by a square cylinder attached with a deformable splitter plate

Cite as: Phys. Fluids **36**, 043612 (2024); doi: 10.1063/5.0200566
Submitted: 27 January 2024 · Accepted: 20 March 2024 ·
Published Online: 15 April 2024

Aravindhan Venkatesh,[1] Jiqiang Niu (牛纪强),[2,3] Xiao Xue (薛骁),[1] Zheng-Wei Chen (陈争卫),[4]
and Hua-Dong Yao (姚华栋)[1,a)]

AFFILIATIONS

[1]Department of Mechanics and Maritime Sciences, Chalmers University of Technology, Gothenburg 42196, Sweden
[2]School of Mechanical Engineering, Southwest Jiaotong University, Chengdu 610031, Sichuan Province, China
[3]Maglev Technology Key Laboratory of Railway Industry, Tongji University, Shanghai 201804, China
[4]Department of Civil and Environmental Engineering, The Hong Kong Polytechnic University, Hong Kong, China

[a)]**Author to whom correspondence should be addressed:** huadong.yao@chalmers.se

ABSTRACT

To understand passive vortex-induced vibrations (VIV) coexisting with active structure motions, this paper numerically investigates the use of pure pitch oscillation to control a square cylinder mounted with a deformable splitter plate at the Reynolds number of 333. The oscillation is enforced with an amplitude of 3° and different frequencies from 0 to 6 Hz. Direct numerical simulations using a partitioned method with a semi-implicit coupling algorithm are performed. According to the trajectories of the splitter-plate tip displacement with respect to the lift or drag force coefficient, a specific lock-in regime determined by the frequency of the enforced pitch oscillation is identified. Further spectral analyses of the tip displacement and lift force show that the lock-in frequencies are equal to the enforced frequencies. Next to the lock-in regime, semi-lock-in regimes with narrow bandwidths are distinguished, exhibiting both lock-in and non-lock-in features. In the non-lock-in regimes, the frequencies of the most predominant peaks in the spectra are found near the natural frequency of the splitter plate of 3.236 Hz, and the frequencies of the two secondary peaks are distributed along the characteristic lines following the ratios of these frequencies to the enforced frequency, which are ±1. Thus, the interaction is dependent on the combined effects of the passive VIV and the actively enforced pitch oscillations. Moreover, the intersection points of the characteristic lines are located close to the upper and lower frequency limits of the lock-in regime, inferring the conditions for the lock-in onset.

I. INTRODUCTION

Vortex-induced vibration (VIV) is a typical phenomenon of fluid–structure interaction (FSI) in flow past a blunt body where vortices induced by the body result in self-sustained vibration of the body. It exists in vast applications such as offshore structures, renewable energy harvesting, biomedical devices, and aircraft. VIV is categorized into flutter, galloping, and buffeting in terms of vibration frequency and amplitudes.[1,2] A benchmark case of VIV is a deformable splitter plate assembled onto the rear side of a square cylinder. Since this configuration setup induces flow possessing plenty of representative mechanisms, it has been widely investigated and considered in the validation of numerical and experimental FSI methods.[3–9]

Matthies and Steindorf[4] proposed an implicit coupling (also termed strongly coupling) algorithm on the basis of a nonlinear block Newton algorithm, to develop a partitioned strategy for FSI simulation. One of the validation cases in their study was the benchmark VIV case of the square cylinder with the splitter plate at the Reynolds number, *Re*, of 333. In the partitioned strategy, the flow and structure deformations were separately solved with different solvers but coupled by iterating variables at the interfaces between the fluid and the structure. Dettmer and Perić[5] took advantage of this benchmark VIV case to validate a partitioned approach with an implicit coupling algorithm. Both flow and solid solvers were implemented based on finite-element discretization. Stabilized low order velocity–pressure finite elements were considered to discretize the incompressible Navier–Stokes equations, and standard finite element approximations for the structure. An arbitrary Lagrangian–Eulerian (ALE) strategy was used to capture the flow domain deformation. A discrete implicit generalized-α method was taken for the temporal discretization of both the solvers. In the study by Wood *et al.*,[7] this benchmark VIV case was simulated using a partitioned approach. An implicit coupling algorithm called the block-Gauss–Seidel (BGS) algorithm was adopted to couple fluid and solid solvers. An incompressible finite volume method (FVM) with an ALE algorithm on deformable fluid–solid interfaces was utilized for the flow solver, and a finite element method (FEM) for large dynamic structural deformation was utilized for the solid solver. Later, considering the same VIV case, Kassiotis *et al.*[8] compared the BGS and explicit algorithms. Habchi *et al.*[9] studied a similar partitioned approach implemented in the open-source tool OpenFOAM and validated the approach based on this benchmark case. The incompressible flow was solved with the PIMPLE algorithm, and the large structural deformation was solved with the Saint Venant–Kirchhoff constitutive model. A dynamic Aitken method was applied to accelerate the coupling iteration between the solvers. Their method has also been tested for a biomechanics application with large deformations by Yao *et al.*[10] A monolithic approach to FSI simulation was proposed by Schott *et al.*[11] One of the cases for the method validation was this benchmark case. In their study, the monolithic approach was implemented for FEM, but it is generally applicable to other discretization schemes.

The square cylinder with the flexible splitter plate has been considered to develop a concept for piezoelectric energy harvesters,[12] where the strain energy from plate deformations is harvested by piezoelectric patches on the polymeric splitter plate. Previous harvesters of this type were installed with rigid splitter plates, which vibrate at relatively higher frequencies. In contrast, the flexible plate of the concept has deformations at low frequencies. Through water-tunnels tests (at Re between 9200 and 14 300) and numerical simulations with a partitioned method coupling the ANSYS modules of Fluent and Mechanical (at Re between 4974 and 9648), Binyet *et al.*[12] showed that the power conversion is dependent on the inflow speed and the geometric parameters such as the square width, and the plate length and thickness. The Reynolds-averaged Navier–Stokes (RANS) equations with the realizable k–ϵ model were used for the flow simulations. In another work of water-tunnel tests by Binyet *et al.*,[13] this configuration at Re from 1500 to 19 700 was studied to understand how the geometric parameters of the splitter plate affect the flow characteristics and, consequently, the harvested mechanical energy.

Instead of a single set of a flexible plate attached on a square cylinder (i.e., the benchmark case reviewed above), Furquan and Mittal[14] analyzed two sets positioned side by side at $Re = 100$ using a partitioned FEM approach. Compared to the single set, this two-set case exhibits out-phase vibrations at the initial stage before in-phase vibrations are developed. The lock-in was found by adjusting the plate structure stiffness but retaining the density ratio of the solid to the fluid and the Poisson ratio. In addition, increasing the distance between the two sets results in a reduced vibration amplitude. Sarioglu[15] carried out an experimental study for a square cylinder at various incidence angles from 0° to 45° at $Re = 3 \times 10^4$, where a rigid and stationary splitter plate with the same length as the square width was positioned behind the cylinder to passively control vortex formation in the wake. It was found that the splitter plate is effective in reducing the drag at all incidence angles. A reduction in 20% is achieved at the zero incidence angle, and the minimum and maximum reductions are near 13° and 20°, respectively.

Aside from the deformable splitter plate, the details of the rigid splitter plate controlling the vortex shedding from the square cylinder within a plane duct at low Re between 110 and 200 were explored numerically by Turki.[16] It was found that the length and location of the splitter plate are critical to affecting the vortex shedding and characteristic Strouhal number, as well as drag and lift coefficients. After that, Ali *et al.*[17] systematically analyzed the effects of attached with of the rigid splitter plate varying between 0.5 and 6 times of the square cylinder width at $Re = 150$ by means of direct numerical simulation (DNS).

In addition to square cylinders, a circular cylinder attached with a deformable splitter plate within a plane channel was put forward as a benchmark VIV case, termed the Turek–Hron benchmark, proposed by Turek and Hron.[18] It has also been widely adopted to validate FSI methods, for example, by Giannelis and Vio.[19] The Turek–Hron benchmark was further modified to generate other VIV cases. For example, in the research by Sahu *et al.*,[20] the circular cylinder was mounted onto a spring so that a spring-mass system at $Re = 150$ was established in addition to the flexible splitter plate. By setting a slip wall condition on the side boundaries and increasing the fluid domain size for the Turek–Hron case, Pfister and Marquet[21] analyzed the FSI stability and dynamics for $Re = 80$. Recently, Tatar and Yao[22] proposed to place an additional circular cylinder upstream of the benchmark and found that this setup enhances the energy harnessing performance of the flexible splitter plate. Duan and Wang[23] conducted the experiments for rigid and flexible plates of different lengths attached to a circular cylinder, to reduce the noise generated from the flow induced by the cylinder at Re from 3.83×10^4 to 9.57×10^4. The effects of cylinder rotation on hydrodynamic forces at low Reynolds numbers were also widely investigated.[24]

Aside from passive VIV, active pitch oscillation was investigated for a NACA0012 airfoil at dynamic stall.[25,26] A suction jet actuator was installed on the airfoil to control flow separation. The operational parameters of the jet were optimized using a genetic algorithm coupled with neural networks. It was found that the optimal jet is effective in improving the aerodynamic performance, since leading-edge and turbulent-separation vortices are suppressed. This inspires that splitter plates can also be used for flow control.

The present study is motivated to understand the interaction between the flow and structural deformation when passive VIV is triggered in combination with active pitch oscillation of the structure. A flexible splitter plate attached to a square cylinder is investigated. This configuration has been simulated in previous studies where the square cylinder is stationary.[3–9,11] In contrast, the square cylinder is enforced to oscillate in the present study. The previous data of the stationary scenario will support the method validation in this study and be used as a reference to address how the enforced oscillation affects VIV. The aim is to explore the effects of the active pitch oscillation on the passive vibrations of the downstream splitter plate. The changes in the lift and drag forces, as well as the structural deformations, will be addressed. Moreover, the onset conditions of the lock-in phenomenon will be understood based on the analysis of variable changes in time and frequency domains. The effects of the enforced pitch frequency will be explored in terms of the predominant flow and structure characteristics.

II. APPLICATION DESCRIPTION

The configuration investigated in this study is shown in Fig. 1. A square cylinder is assembled with a splitter plate at the center of the backside of the cylinder. The square cylinder is rigid, whereas the

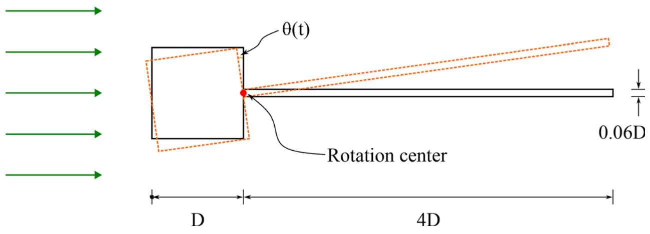

FIG. 1. Schematic of the flexible splitter plate attached to the square cylinder, where the cylinder is enforced to oscillate. The arrows upstream of the body indicate the inflow direction. The angle $\theta(t)$ varies periodically in time.

splitter plate is flexible. The side length of the square cylinder is D, and the plate has a length of $4D$ and a thickness of $0.06D$.

This combined structure system is forced to oscillate periodically at the center of the joint between the square cylinder and the splitter plate. The time-varying pitch angle is defined as

$$\theta = A\sin(2\pi f_{exc}t)\ , \tag{1}$$

where the pitch angle amplitude is $A = 3°$, and the oscillation frequency f_{exc} is prescribed between 0 and 6 Hz. This frequency range is chosen in order to encompass the first natural frequency of the splitter plate, $f_{n,1}$, which is reported in Table III in Sec. V A.

The setup of the configuration and inflow conditions are established in reference to a benchmark VIV configuration at Re = 333 where the square cylinder is stationary. Here the Reynolds number (Re) is calculated based on the side length of the square body, D, and the free-stream flow velocity, U_0. The benchmark configuration at Re = 333 has been computed in two-dimensional (2D)[3–6,9,27] and three-dimensional (3D) simulations.[7] In addition, this benchmark configuration at Re = 204 was simulated in 2D.[28,29] The DNS was used in the simulations at both the Reynolds numbers.

The present flow is specified at Re = 333 by following the previous studies.[3–7,9,27] In the study conducted by Wood *et al.*,[7] the flow was simulated in 3D, while the structure of the splitter plate was modeled in 2D using a neo-Hookean plane stress material. Their results are consistent with others, where both the flow and the structure are computed in 2D.[3–5] It is known that flow past a circular cylinder at Re larger than 188.5 exhibits secondary instability along the spanwise direction.[30,31] Similarly, such instability should also exist for the square cylinder in the present cases, which needs to be resolved using 3D simulations. However, according to the results of Wood *et al.*,[7] the secondary instability has a negligible effect on affecting the current VIV system. The reason is that the 2D structure modeling suppresses the spanwise structural deformation. Based on this finding, the present cases are simulated with the 2D approximation. The available data for Re = 333[3–7,9,27] will be used for the methodology validation in Sec. III. However, the forced oscillation has not been introduced in these previous studies.

The incompressible flow is defined since the free-stream Mach number of 0.151 is much smaller than the critical value of 0.3. The characteristic frequency of the flow passing over the square body is $f_T = U_0/D = 51.3\,\text{Hz}$.

The splitter plate is regarded as linear elastic. As the square cylinder is rigid, it has no deformations and is thus excluded from the structural analysis. The reduced velocity ratio is defined as $U_0/(f_{n,1}D) = 1.542$, where $f_{n,1}$ is the first natural frequency of the splitter plate. The mass ratio of the plate structure density to the fluid density is 84.756. The mass ratio is chosen to ensure a limited added mass effect in the current VIV system in consideration of the low free-stream flow velocity and the splitter-plate tip velocity. As reported by Sahu *et al.*,[20] the structural vibration amplitude and frequency are not changed much against the mass ratio, when it is larger than 10 and the reduced velocity ratio is smaller than 2. The VIV system in their study is a flexible splitter plate (of different lengths from $1.5D$ to $3.5D$) attached to a cylinder with passive vertical oscillation (VO) at $Re = 150$. A similar effect was also found for a single VO cylinder and for a rigid splitter plate attached to a VO cylinder.[32] As the different VIV systems exhibit the common effect, it is deduced that the mass ratio specified in this study can lead to small added mass. Nevertheless, a research in the future is to address the influence of the mass ratio. Young's modulus of the plate is 2.5×10^5 Pa, and the Poisson ratio is 0.35.

III. NUMERICAL METHOD

A. Governing equations

The governing equations of the continuity and momentum in the 2D incompressible flow are written as

$$\frac{\partial u_i}{\partial x_i} = 0, \tag{2}$$

$$\frac{\partial u_i}{\partial t} + u_j\frac{\partial u_i}{\partial x_j} = -\frac{1}{\rho_f}\frac{\partial P}{\partial x_i} + \nu\frac{\partial^2 u_i}{\partial x_j \partial x_j}, \tag{3}$$

where u_i and u_j denote the i- and j-indexed components of the velocity vector, respectively. P is the pressure. The density ρ_f is constant for the incompressible flow. The kinematic viscosity is denoted by ν.

The structure material is linear elastic and isotropic. In the structural model, the effects of gravity and structural damping are neglected. The momentum balance equations in the Lagrangian form read

$$\frac{\partial^2 y_i}{\partial t^2} = \frac{1}{\rho_s}\frac{\partial \sigma^s_{ij}}{\partial x_j}, \tag{4}$$

where y_i- is the i-indexed component of the displacement vector, ρ_s is the structure density, and σ^s_{ij} denotes the second-order Cauchy stress tensor. The Saint Venant–Kirchhoff model is used to take into account the geometric nonlinearity that is caused by large structure deflection.[33] The constitutive stress–strain relationship of the linear elastic model deals with the Green–Lagrange strain tensor G_{ij}:

$$G_{ij} = \frac{1}{2}\left(\frac{\partial y_i}{\partial x_j} + \frac{\partial y_j}{\partial x_i} + \frac{\partial y_k}{\partial x_i}\frac{\partial y_k}{\partial x_j}\right)\ . \tag{5}$$

The second Piola–Kirchhoff stress tensor is written as

$$S_{ij} = \frac{1}{2}E\left(\frac{1}{(1+\nu_s)}G_{ij} - \frac{\nu_s}{(1+\nu_s)(1-2\nu_s)}G_{kk}\delta_{ij}\right)\ , \tag{6}$$

where E is Young's modulus, and ν_s is Poisson's ratio.

B. Partitioned approach of coupled FSI

The simulation of FSI adopts a partitioned approach.[34] In this approach, the fluid and structure are solved separately using different solvers. An ALE algorithm is utilized to describe the continuum mechanics in the progression of the deforming fluid and structure domains in time and space.[35,36] A semi-implicit method is applied to coupling the fluid and structure solvers.[37,38] The flow pressure and shear stress tensors are exchanged with the structure displacements on the interfaces between the flow and structure domains, where a space conservative interpolation approach is used to map these variables onto unconformable mesh cells between the domains.[39]

In the flow solver, a finite volume method based on the pressure-based segregated algorithm of semi-implicit method for pressure linked equations (SIMPLE) is used.[40] A least squares cell-based approach is adopted in the computation of gradients. A second-order upwind scheme is used in the spatial discretization of the momentum equations. The time marching approach is implemented with an implicit scheme. The threshold value of residuals for justifying convergence per time step is set to 1×10^{-6}.

The structure solver utilizes the finite element method (FEM).[41] The approximation of the discretized governing equations in a weak form is derived on the basis of the Galerkin method of weighted residuals.[42] The element approximation chooses the same formulations for the weighting and element shape functions. The Gaussian integration method is used to calculate integrals.[43] Dynamic simulation is performed since the splitter-plate structure is subjected to transient dynamic loads from the flow.

C. Numerical setup

The computational domains of the fluid and structure are sketched in Fig. 2. The domain dimensions and layout are defined in reference to the studies by Ramm and Wall[44] and Bazilevs *et al.*[45] The lengths are normalized based on the square cylinder width *D*. The inlet is positioned for 4.5 from the square cylinder, the side boundaries for 5.5, and the outlet for 14. To monitor the flow field, three probes such as S1, S2, and S3 are positioned at $(x, y) = (0.5, 0.5)$, (8, 0), and $(0.5, 0.8)$, respectively.

In the flow simulation, the boundary condition (BC) of the velocity inlet is set at the inlet of the flow domain, the symmetry BC is set at the side boundaries, and the pressure outlet at the outlet. The under-relaxation factors for the pressure and momentum in the segregated flow solver are set to 0.3 and 0.7, respectively. In the structure domain, the time-varying rotation, which is predefined in Eq. (1), is set at the center of the joint surface between the square cylinder and the splitter plate.

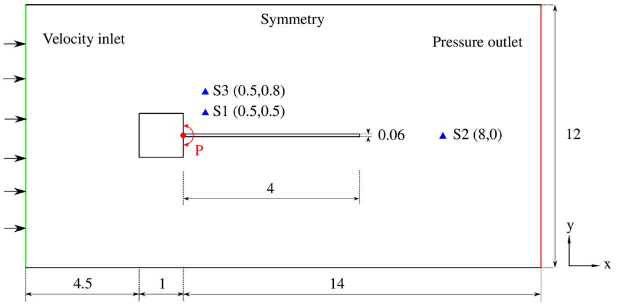

FIG. 2. Schematic of the fluid and structure computational domains. The dimensions are normalized based on the square cylinder width *D*. The triangles mark out the probe positions such as S1, S2, and S3 for monitoring flow variables.

A desktop computer with the Intel® Core™ i9-9900 Processor was used to run parallel simulations. The CPU has 8 cores of 16 threads. The physical memory of the desktop computer is 64 GB. The operating system is Microsoft Windows 11.

IV. METHOD VALIDATION

A. Mesh independence study

Structured meshes are generated in the fluid and structure domains. The Laplacian method is used to update the meshes during the simulation. The dimensionless key cell sizes of the baseline case, normalized by the square body length *D*, are listed in Table I. The surface cell sizes for the splitter plate are taken to generate both the fluid and structure meshes, and the remaining parameters for the generation of the fluid mesh. The growth ratio of the cell sizes in the fluid mesh is 1.1. The surface cell size on the side surfaces of the splitter plate ranges between 0.03 and 0.08. There are 20 layers of hexahedral elements within the plate.

A convergence study of the mesh resolution is carried out based on the meshes in Table II. There are five meshes, meshes 1–5, with different grid resolutions. These meshes are globally coarsen or refined with a refinement factor (RF) in reference to the baseline mesh—mesh 3 outlined in Table I. Moreover, it is of interest to understand whether the time step is small enough to provide converged results. Three values of the time step are set for mesh 3. Another factor that might impact the simulation accuracy is the modeling of the geometric nonlinearity for the structure.[33] To clarify this impact, the nonlinear model is switched on or off for mesh 3 with the different time step values, namely, cases a–f for mesh 3 in Table II. The maximum Courant–Friedrichs–Lewy (CFL) numbers of all cases are less than 1. Considering the largest time step of $\Delta t/T = 5.13 \times 10^{-2}$ for mesh 5, the maximum CFL number is 0.36. As the cell sizes of mesh 5 are smaller than the other meshes, its maximum CFL number is the largest among the cases.

The convergence is evaluated in terms of the maximum displacement of the splitter plate tip in the direction normal to the free-stream flow direction, $y_{tip,max}$, and the frequency of the energy peak in the power spectral density (PSD) of the splitter-plate tip displacement, f_{res}. Fast Fourier transformation (FFT) is used for the PSD calculation. The total length of the signals is 160*T*, where *T* is the time of the flow passing over the square cylinder. Each signal is divided into 15 segments, with an overlapping rate of 50%. The sampling frequency is 1000 Hz. The Hanning window is used as the window function.

TABLE I. The normalized key cell sizes of the baseline case (i.e., mesh 3 in Table II).

Location	Size
Square body surface	0.026–0.05
Splitter plate surface[a]	0.03–0.08 (side) 0.003 (tip)
First-layer cell height near walls	0.002
Far-field boundary	0.34
Growth ratio of cell sizes	1.1

[a] As the splitter plate surface is actually the FSI interface, the cell sizes are used for both fluid and structure meshes.

TABLE II. Results from different grid resolutions and numerical setups compared with the previous studies.[a]

Mesh number	RF	N_{tot}	LD	$\Delta t/\mathrm{T}$	$y_{tip,max}/D$	f_{res} (Hz)
Mesh 1	0.6	4274	Yes	5.130×10^{-2}	1.0773	3.3630
Mesh 2	0.8	6740	Yes	5.130×10^{-2}	1.0529	3.3390
Mesh 3-a	–	9408	Yes	5.130×10^{-2}	1.0430	3.3270
Mesh 3-b	–	9408	No	5.130×10^{-2}	1.0867	3.2723
Mesh 3-c	–	9408	Yes	2.565×10^{-2}	1.0264	3.2971
Mesh 3-d	–	9408	No	2.565×10^{-2}	1.1028	3.2175
Mesh 3-e	–	9408	Yes	1.026×10^{-2}	1.0254	3.2798
Mesh 3-f	–	9408	No	1.026×10^{-2}	1.1349	3.1867
Mesh 4	1.2	12 520	Yes	5.130×10^{-2}	1.0345	3.2990
Mesh 5	1.4	19 738	Yes	5.130×10^{-2}	1.0393	3.2560
Wall[3]					1.12–1.32	2.78–3.26
Matthies and Steindorf[4]					1.0–1.35	3.13
Dettmer and Perić[5]					1.1–1.4	2.96–3.31
Olivier *et al.*[6]					0.95	3.165
Wood *et al.*[7]					1.1–1.2	2.78–3.13
Habchi *et al.*[9]					1.02	3.253

[a] Here, RF is the refinement factor, N_{tot} the total number of cells, $y_{tip,max}$ the maximum displacement of the splitter plate tip, and f_{res} the frequency of the plate structure response. The large deflection (LD) is switched on or off. The blue frame highlights the final choice used for the following analysis, that is, the baseline mesh in Table I.

By comparing the cases of meshes 1, 2, 3-a, 4, and 5 with the same settings such as the large deflection and $\Delta t/T = 5.13 \times 10^{-2}$ in Table II, the maximum plate tip displacement $y_{tip,max}$ and the peak frequency f_{res} are well converged with respect to the mesh resolution. In reference to mesh 3-a of $y_{tip,max}/D = 1.043$, the deviations from the fine meshes (meshes 4 and 5) are 0.0085 and 0.0037. A similar convergence is also observed for f_{res}, which is 3.327 Hz in mesh 3-a. Meshes 4 and 5 deviate from mesh 3-a by –0.028 and –0.071 Hz, respectively.

Define the time-averaged absolute value of the splitter-plate tip displacement as

$$\bar{\psi} = \frac{1}{t_1 - t_0} \int_{t_0}^{t_1} |y_{tip}| dt \ , \tag{7}$$

where t_0 is the time when the flow is fully developed, and $(t_1 - t_0) = 226T$. In reference to the results from the finest mesh resolution (mesh 5), the error of $\bar{\psi}$ from mesh i (for i = 1, 2, 3-a, 4) is defined as

$$\% \ e_{\bar{\psi}}|_{\mathrm{Mesh\ i}} = \frac{(\bar{\psi}|_{\mathrm{Mesh\ i}} - \bar{\psi}|_{\mathrm{Mesh\ 5}})}{\bar{\psi}|_{\mathrm{Mesh\ 5}}} \times 100\%. \tag{8}$$

By replacing $\bar{\psi}$ with f_{res} in Eq. (8), the error of f_{res} from mesh i is defined similarly.

Based on Eq. (8), the errors of $\bar{\psi}$ and f_{res} from the different mesh resolutions are plotted in Fig. 3, where mesh 3 corresponds to mesh 3-a in Table II. As can be seen, the errors decay exponentially with respect to the total number of cells N_{tot}. The trends suggest that the independence of the mesh resolution is achieved.

The influences of the geometric nonlinear structural modeling[33] are identified through the comparison of the cases on the basis of mesh 3. The modeling is considered in cases 3-a, 3-c, and 3-e with the different time step sizes, but excluded from the other cases. According to the results in Table II, disregarding the modeling leads to differences in $y_{tip,max}$ and f_{res}, which are not negligible. Therefore, the nonlinearity associated with large deformations of the splitter plate is important for numerical accuracy. The modeling is involved in the simulations in the following analysis of the VIV.

The time step size is adjusted in cases 3-a–3-f of mesh 3 to find a feasible value. The results of cases 3-a, 3-c, and 3-e, where the geometric nonlinear structure model is accounted for, show limited differences between them. Case 3-a with $\Delta t/T = 5.13 \times 10^{-2}$ provides

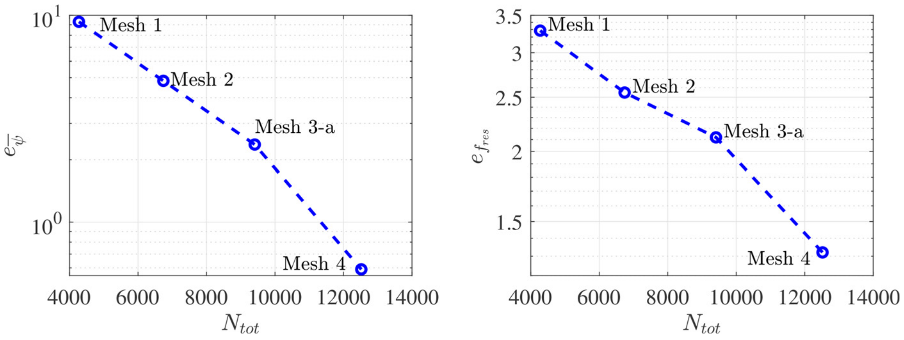

FIG. 3. The errors of the time-averaged absolute tip displacement $\bar{\psi}$ and the peak frequency of the tip displacement f_{res} from the different mesh resolution in reference to the finest mesh (mesh 5) as a function of the total number of cells N_{tot}.

$y_{tip,max}/D = 1.043$, whereas cases 3-c and 3-e with smaller time step sizes provide 1.0264 and 1.0254, respectively. Moreover, f_{res} of case 3-a is 3.327 Hz, which is similar to the other cases of 3.2971 and 3.2798. In addition to that, although the geometric nonlinear model is excluded from cases 3-b, 3-d, and 3-f, the results of these cases with different time step sizes are similar. It is, therefore, reasonable to choose the time step size of $\Delta t/T = 5.13 \times 10^{-2}$ to guarantee numerical accuracy and a relatively shorter simulation time.

The cases of this study are also compared to the same scenario (i.e., the same configuration at $Re = 333$) simulated in previous studies,[3–7,9] as listed in Table II. The present cases give $y_{tip,max}/D = 1.0254$–1.1349 and $f_{res} = 3.1867$–3.363 Hz. These values are consistent with the previous results.

V. RESULTS AND DISCUSSION

A. Modal analysis

A model analysis is performed for the flexible splitter plate using FEM and an analytical modeling method, i.e., the Euler–Bernoulli beam model.[46] It is assumed that there are no external forces, structural, or viscous damping effects. In the analytical model, the general form of the nth mode shape reads

$$\phi(x) = A\sin(\beta_n x) + B\cos(\beta_n x) + C\sinh(\beta_n x) + D\cosh(\beta_n x), \quad (9)$$

$$\beta_n^4 = \omega_n^2 m/(EI) \ , \quad (10)$$

where m is the mass per unit length of the splitter plate, I is the area moment of inertia of the plate section, and ω_n is the natural circular frequency. Given the upstream tip of the plate is imposed with zero displacement and rotation, β_n at the downstream tip of the plate satisfies

$$\cos(\beta_n L)\cosh(\beta_n L) + 1 = 0 \ , \quad (11)$$

where L denotes the length of the splitter plate. Equation (11) is solved analytically to determine ω_n.

The first three natural frequencies of the splitter-plate structure ($f_{n,1}$, $f_{n,2}$, and $f_{n,3}$), which are computed using the two methods, are presented in Table III. In the FEM simulation, mesh 3 is adopted. The FEM results are consistent with those of the analytical model. Small differences of about 6% between the methods are observed.

B. Unsteady FSI characteristics

Lift and drag forces of the configuration including both the square body and the splitter plate are analyzed by means of the trajectory evolution of the force coefficients in time. The lift coefficient is defined as $C_L = f_y/(0.5\rho_f U_0^2)$, and the drag coefficient is defined as $C_D = f_x/(0.5\rho_f U_0^2)$. The trajectory evolution of C_L against C_D for a variety of active oscillation frequencies f_{exc} is shown in Fig. 4. Here f_{exc} ranges between 0 and 6 Hz. The time-averaged drag coefficient $C_{D,mean}$ and the root mean square (RMS) value of the lift coefficient $C_{L,RMS}$ are marked out in this figure.

TABLE III. Natural frequencies of the flexible splitter plate (unit: Hz).

Natural frequency	Analytical model	FEM
$f_{n,1}$	3.0288	3.2360
$f_{n,2}$	18.981	20.256
$f_{n,3}$	53.148	56.628

As shown in Fig. 4, the polar of C_L and C_D evolves in a closed simple trajectory as the square body is stationary, i.e., $f_{exc} = 0$ Hz. However, as f_{exc} is slightly increased to 0.25 Hz, the trajectory becomes disordered. It is enveloped within a region that has a similar overall shape but is larger compared to that of the stationary case. This suggests larger lift and drag variations are introduced by the enforced body oscillation. The disordered status is sustained until f_{exc} increases up to 2.75 Hz. The area spanned by the trajectory is increased with f_{exc}. A special case is found at 2.25 Hz, where the trajectory is comparatively less complex than the neighbor frequencies.

Clear single trajectories are also observed at $f_{exc} \in [2.875, 3.5]$ Hz in Fig. 4. This phenomenon indicates that a lock-in effect appears because of the interaction between the plate structure and flow. The variation range of the trajectory is decreased as the frequency increases. The trajectory is almost collapsed into a curve at 2.875 Hz, while it becomes separated to form a butterfly shape at higher frequencies. The shapes of the trajectories at these high frequencies are different from that of the stationary case.

For f_{exc} above 3.5 Hz, Fig. 4 shows that disordered trajectories are excited again. The trajectory variation range first increases with respect to f_{exc} up to 4.25 Hz and then decreases with the frequency. This behavior is different compared to the disordered cases at the lower frequencies before the lock-in regime onsets, as discussed above. Moreover, the variation range at 3.625 Hz after the lock-in regime is much smaller than that at 2.75 Hz before the lock-in regime, but is relatively comparable to 0.25 and 6 Hz. A relatively less complex trajectory is seen at 4.5 Hz outside the lock-in regime. A similar effect also exists at 2.25 Hz below the lock-in frequencies.

The evolution history of the trajectories of the splitter-plate tip displacement, y_{tip}, and the lift coefficient, C_L, is displayed in Fig. 5. As can be seen, the trajectory of the stationary-cylinder case at $f_{exc} = 0$ Hz does not follow a single loop. This behavior is contrary to the lift-drag trajectory identified in Fig. 4. A reason is that vortices bring about velocity and force fluctuations at high frequencies, which will be discussed later in spectral analysis.

It is clear in Fig. 5 that the trajectory becomes regularized as a single closed loop in the lock-in regime of $f_{exc} \in [2.875, 3.5]$ Hz. Moreover, at 2.875 Hz where the lock-in regime onsets, the tip displacement is zero meter (i.e., at the neutral position of the splitter plate) when the lift force coefficient is zero. In contrast to this effect, at the other higher frequencies of the lock-in regime, the zero tip displacement is associated with non-zero lift coefficients. There are two points in the trajectory curve where the tip displacement is zero. They are dependent on the sides from which the plate returns to the neutral position. In addition, the trajectories at 2.25 and 4.5 Hz are less disordered than the neighboring frequencies, although both frequencies are away from the lock-in regime. These behaviors agree with the findings for the lift-drag trajectories in Fig. 4.

Figure 6 displays the evolution history of the trajectory from the tip displacement and the drag coefficient C_D. The stationary case at $f_{exc} = 0$ Hz also exhibits a simple trajectory. This is in line with the observation for the displacement vs C_L in Figs. 4 and 5, since flow vortices affect the drag and lift forces simultaneously.

A general observation in Fig. 6 is that the smallest C_D always appears at two positions of the plate tip that are located between the neutral and the maximum positions, but not at the neutral position. The reason is that vortices are subjected to fewer constraints in the

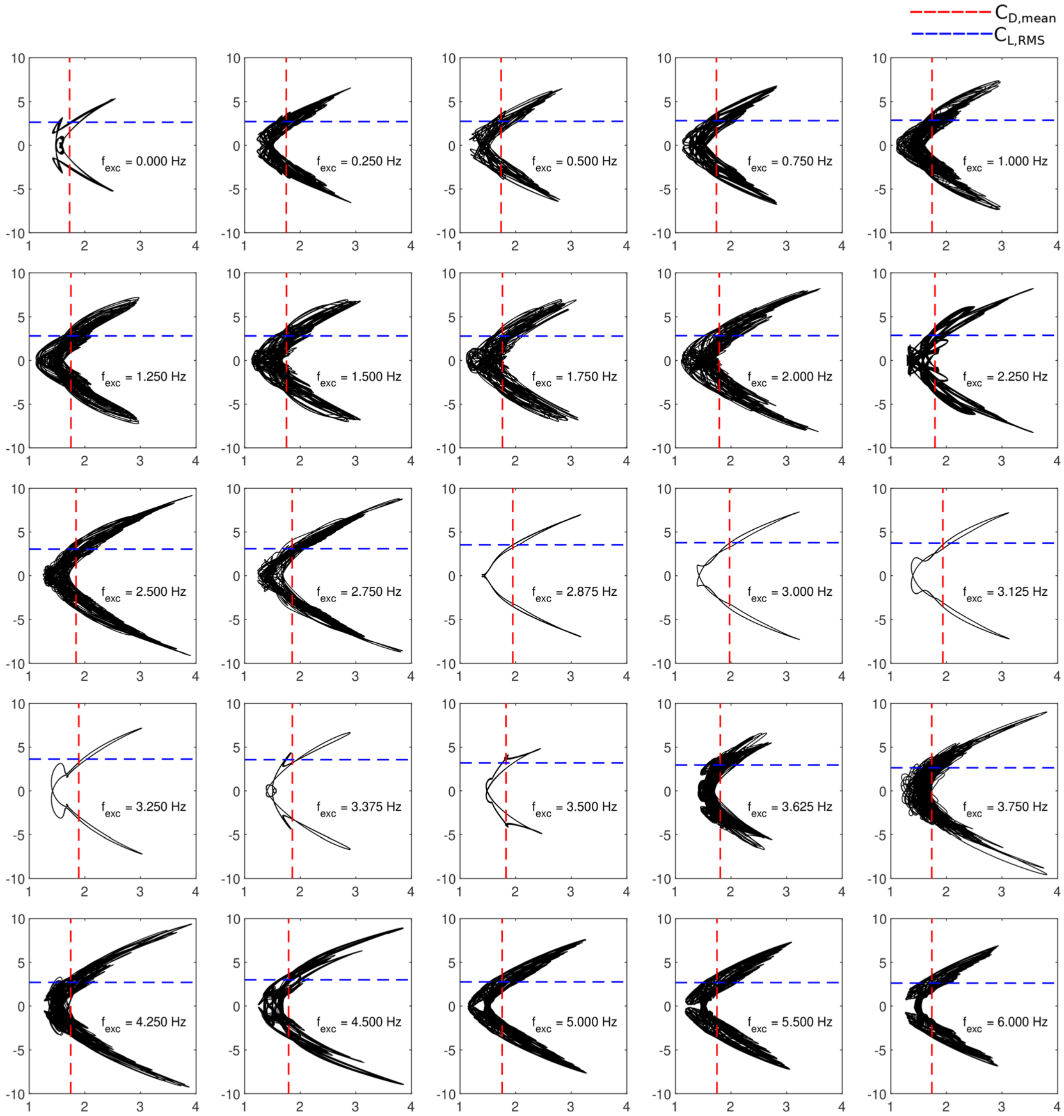

FIG. 4. The trajectory evolution of C_L vs C_D in time. The x-axis is C_D, and the y-axis is C_L. The red and blue dash lines mark out $C_{D,mean}$ and $C_{L,RMS}$.

process of being swept downstream, when the splitter plate is pitched away from the neutral position. Furthermore, C_D increases rapidly as the plate tip approaches to the maximum deformation position, while it has the largest value before the plate tip reaches to the maximum position. This process indicates that the streamwise motion of vortices is confined by the pitch plate, resulting in the impingement of the vortices onto the plate. The impingement is increased quickly when the pitch process approaches the largest plate deformation.

As shown in Fig. 6, because of the lock-in, single close trajectories are seen at the enforced frequencies between 2.875 and 3.5 Hz. This effect is well consistent with the findings in Figs. 4 and 5. It is noticed in Fig. 6 that the area spanned by the trajectory increases with the enforced frequency before the lock-in regime is reached. Then, in the lock-in regime, it grows with frequencies up to 3.125 Hz and then is narrowed down. After the regime, the area becomes larger again up to 4.5 Hz and decreases above this frequency. Additionally, the trajectories at 2.25 and 4.5 Hz are less disordered than the neighboring frequencies. These phenomena agree with those in Figs. 4 and 5.

Snapshots of the z-component of the vorticity vector, ω_z, for several selected f_{exc} are illustrated in Fig. 7. These frequencies are 0, 2, 3.125, 4.25, and 6 Hz, which spread over the whole frequency range of interest including the lock-in regime. The contours at the different oscillation frequencies exhibit similar vortex patterns. This indicates that given the pitch oscillation amplitude and Reynolds number in this study, the flow mode of vortices detached from the square body is not sensitive to the oscillation frequencies. However, the structural responses to the flow are highly dependent on the oscillation frequencies, since the splitter plate is enforced to interact with the vortices.

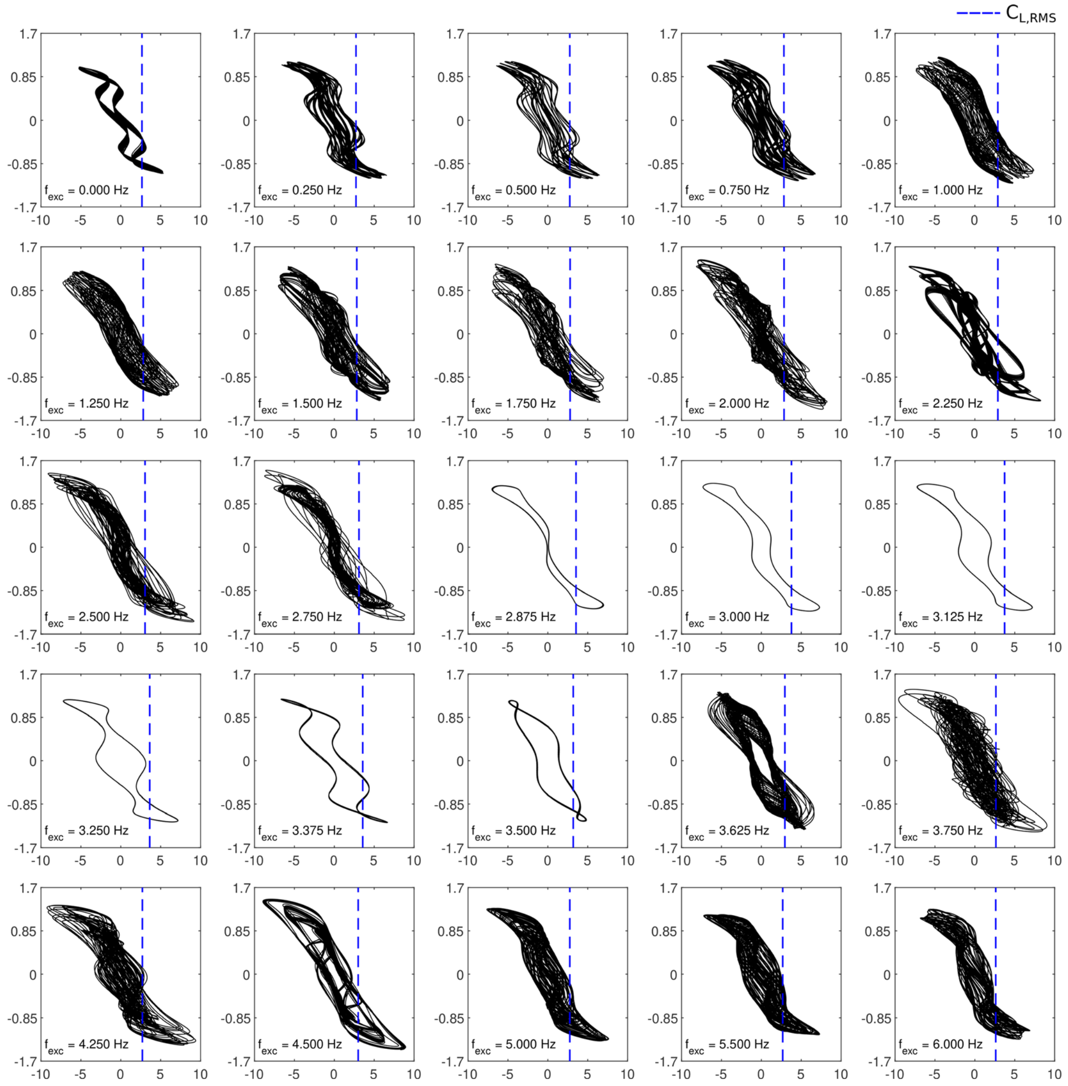

FIG. 5. The trajectory evolution of y_{tip}/D vs C_L in time. The x-axis is C_L, and the y-axis is y_{tip}/D. The blue dash line indicates the RMS value of C_L.

This effect is identified in the preceding trajectory analysis of the force coefficients and splitter-plate tip displacement, which behave in distinct manners within and outside the lock-in regime.

The time series of the tip displacement y_{tip} and the velocity component u_y, which is normal to the free-stream flow direction, at the probe point S2 are displayed in Fig. 8. The results of $f_{exc} = 0$, 2, 3.25, and 4.25 Hz are chosen to show. Assuming the splitter plate is rigid without any deformation, periodic sinusoidal displacement at the plate tip is obtained and also shown in the figure to explore the potential coherence between the passive structure deformation and the active (enforced) structure oscillation (i.e., the pitch motion). The probe point is positioned in the wake downstream of the plate, and its coordinates are found in Fig. 2.

It is seen in Fig. 8 that the plate tip in the stationary case exhibits regular wavy displacements. The velocity component u_y in the wake in this case, however, fluctuates with an irregular wave shape, indicating that multiple frequencies exist in the fluctuations.

In the cases of the square cylinder enforced with $f_{exc} = 2$ and 4.25 Hz outside the lock-in regime in Fig. 8, y_{tip} fluctuates with a variety of amplitudes and phases, which does not follow the enforced oscillation displacement (drawn with the red curves in the figure). The tip displacement in the case at 4.25 Hz shows more wave periods than that at 2 Hz. It suggests that the enforced pitch oscillation introduces fluctuations at more frequencies. Meanwhile, the fluctuations of u_y are much more irregular in both cases.

A specific case shown in Fig. 8 is the one at $f_{exc} = 3.25$ Hz, which is located within the lock-in regime. As can be seen, the tip displacement fluctuates in a regular waveform. A constant phase shift is identified in the plate tip displacement in comparison to the enforced tip oscillation. The amplitude of the tip displacement is much larger than

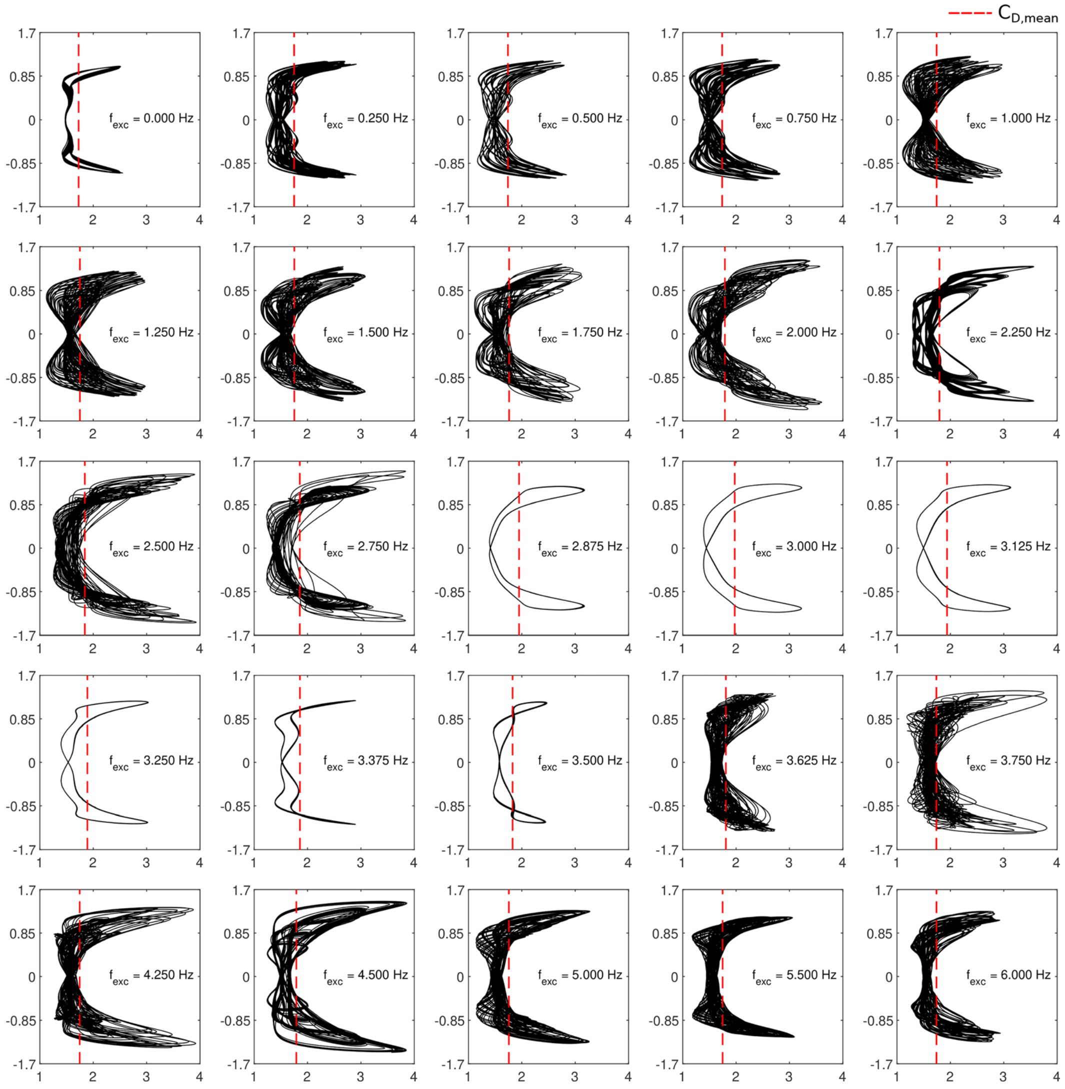

FIG. 6. The trajectory evolution of y_{tip}/D against C_D in time. The x-axis is C_D, and the y-axis is y_{tip}/D. The red dash line indicates the time-averaged value of C_D.

the enforced tip oscillation, since the large-scale deformation of the flexible plate accounts for additional displacement at the plate tip. Moreover, the velocity component u_y at S2 in the wake exhibits periodic wave-like fluctuations. Small fluctuations are observed near the wave troughs and valleys. This implies the fluctuations at a relatively higher frequency because of vortices developed in conjunction with the upstream structure vibration.

C. Spectral analysis of FSI

The normalized PSDs of the velocity component u_y (denoted by $\hat{S}_{u_y}$) at the probe points, S1, S2, and S3, for several cases are shown in Fig. 9, where the predominant peaks and corresponding frequencies are marked out. All PSDs in the different cases are normalized based on the maximum peak of S2 at 3.327 Hz in the stationary case ($f_{exc} = 0$ Hz). The coordinates of the probe points are illustrated in Fig. 2. As noticed in Fig. 7, S1 is placed between two shear layers that are shed from the leading and trailing edges of the square body, respectively. The position of S3 is mainly inside the region over which the leading-edge vortices pass. S2 is contained in the wake downstream of the splitter plate.

In the stationary case in Fig. 9, two predominant peaks are observed at S1. The maximum peak at 6.653 Hz, and the smaller peak exists at 3.327 Hz, which is close to the first natural frequency of the splitter-plate structure of $f_{n,1} = 3.236$ Hz. The smaller peak frequency is half of the other large peak frequency. The same maximum peak frequency at 6.653 Hz is also seen for S3. Despite a peak at 3.327 Hz also exists at S3, its normalized magnitude is nearly negligible than that at S1. Looking at S2, only one peak is recognized at 3.327 Hz. The results convey that the shear layer mainly contains vortices at the two

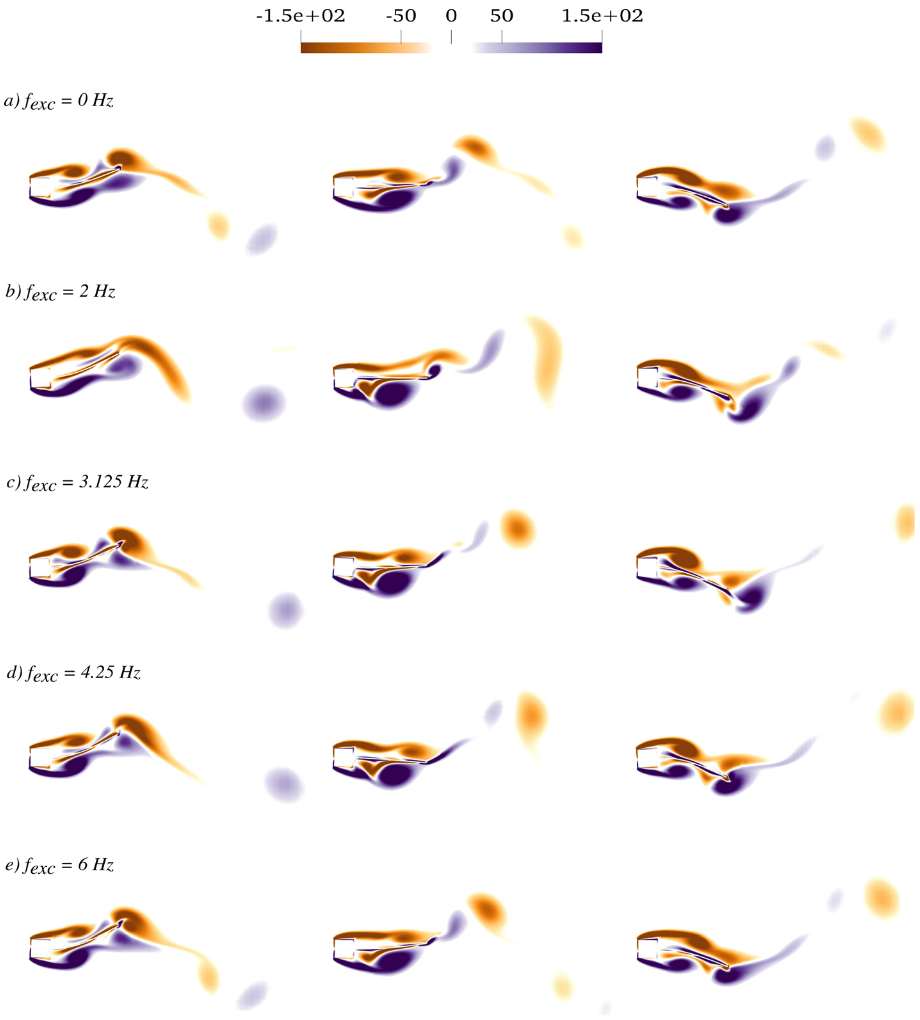

FIG. 7. Snapshots of the vorticity component ω_z. From left to right: approximately the position of the maximum tip displacement, the neutral position, and the position of the minimum tip displacement.

frequencies identified in the PSDs. The vortices at the lower frequency are flushed down along the splitter plate and then excite the plate vibration. Meanwhile, when the other vortices at the higher frequencies move downstream, they go outward away from the splitter plate and, therefore, have a limited influence on the plate vibration. This effect is visualized in terms of the vorticity component ω_z in Fig. 7. The probe point, S1, is in the region where the leading- and trailing-edge shear layers interact with each other, and the leading-edge vortices occur on the outer side with respect to those trailing-edge ones. Therefore, it is reasonable to deduce that S1 captures the characteristic frequencies of both shear layers, namely, the two predominant peak frequencies. S3 presents the characteristic frequency of the leading-edge shear layer. At S2, the vortices from the two sides of the square body merge together, and the merged wake is characterized with a peak frequency of 3.327 Hz.

In Fig. 9, the enforced case with $f_{exc} = 2$ Hz shows five significant peaks at S1. The multiple frequencies arise as the enforced frequency is outside the lock-in regime. Part of these frequencies such as 3.245 Hz is only identified at S2, and the others (5.245, 6.469, and 8.469 Hz) as well as 7.245 Hz are identified at S3. This phenomenon suggests that S1 captures the flow characteristics at both S2 and S3. This effect is also found in the stationary case discussed above. By observing the enforced cases with $f_{exc} = 3.25$ in the lock-in regime and 4.25 Hz above the regime, the same effect exists as well.

To understand the effects of the enforced pitch frequency on the characteristic frequencies of the tip displacement and the lift and drag forces, the PSDs of these variables are shown in Fig. 10. The results of each variable are normalized based on the largest peak magnitude of the respective PSD in the stationary case. As can be seen in the stationary case, the PSD of the lift force $\hat{S}_L$ shows another smaller peak at 16.653 Hz, in addition to the peak at 3.327 Hz that is also observed for the velocity field in Fig. 9. The drag force $\hat{S}_D$ has three peaks. The additional small high frequency peaks explain the reason about why the trajectories in Figs. 4–6 are not completely single loops. Similar phenomena are observed for the enforced cases, so the trajectories related to the lift and drag become disordered. Among all variables, the PSDs of the drag force exhibit more peaks than the tip displacement and lift force. This might be caused by the splitter plate interfering the shear

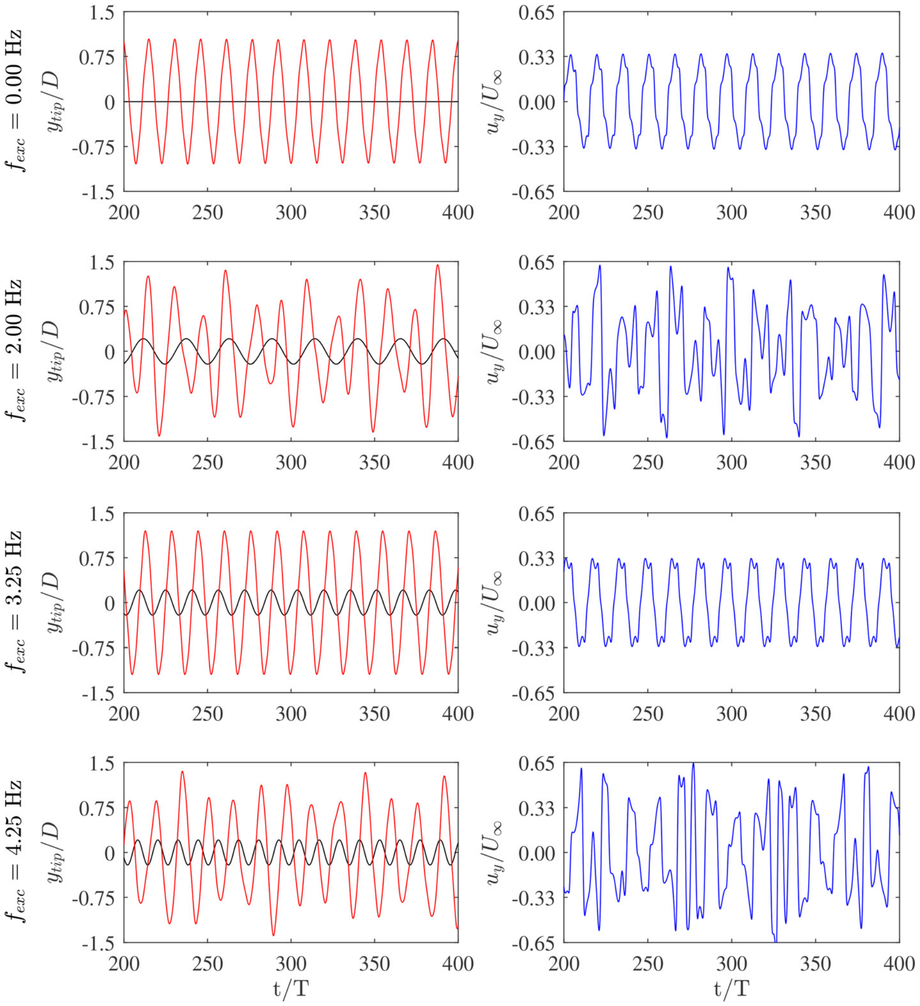

FIG. 8. The time series of the normalized tip displacement y_{tip}/D and the normalized velocity component u_y/U_∞ at the probe point, S2, in the wake. The black curves in the left figures indicate the tip displacement of a rigid splitter plate.

layers detached from the leading edges of the square cylinder (see Fig. 7). A common effect in all cases is that the frequency of the major peak is near the natural frequency of the plate. However, for the enforced frequencies of f_{exc} at 2.75 and 3.75 Hz, which are close to the lock-in regime, the tip displacement is noticed with another peak with a large magnitude that exists near f_{exc}, and the lift force also presents a relatively large peak at the same frequencies. It means that the flow and structure interact at two characteristic frequencies. Thus, the trajectory of the tip displacement and lift force becomes disordered, as found in Fig. 5. A special case is at $f_{exc} = 3.625$ Hz, which is the upper bound of the lock-in regime. Only one significant peak exists for both the tip displacement and the lift force, but several very small peaks commence. This leads to a disordered trajectory as well. When $f_{exc} = 0.25$ and 5 Hz, which are far from the lock-in regime, secondary peaks at the enforced frequencies become small.

In Fig. 11, the RMS lift coefficient $C_{L,RMS}$, the time-averaged drag coefficient $C_{D,mean}$, and the RMS drag coefficient $C_{D,RMS}$ are plotted as a function of f_{exc}. All the three coefficients change in similar trends: the magnitudes gradually increase and reach the largest value at $f_{exc} = 3$ Hz. Above this frequency, the magnitudes drop fast to become similar to that in the stationary case. Recalling the lock-in regime for $f_{exc} \in [2.875, 3.5]$ Hz indicated in Fig. 4, it is, therefore, found that the fast increase and drop of the large magnitudes are triggered due to the lock-in effect. The large RMS values of the lift and drag coefficients imply that flow vortices and structure deformations are intensively interacted at specific frequencies. Therefore, remarkable energy from the flow is absorbed by the splitter-plate structure. It is worth noting that the frequency of the largest coefficient is 3 Hz rather than 3.25 Hz that is closer to the first natural frequency of the splitter plate $f_{n,1} = 3.236$ Hz. The reason is associated with the combined effects of the passive VIV and active pitch oscillation, which will be explained in the following discussion. Moreover, another obvious increase starting from 4.25 Hz outside the lock-in regime is observed and leads to a local maximal magnitude at 4.5 Hz. Above this frequency, the coefficients decrease, even though the enforced oscillation is enhanced by increasing f_{exc}.

Figure 12 shows the dominant peak frequencies obtained from the normalized PSDs of the lift force, $\hat{S}_L$, in the enforced oscillation frequency range between 0 and 6 Hz, and the symbols plotted are colored based on the normalized peak magnitudes. The normalization is made

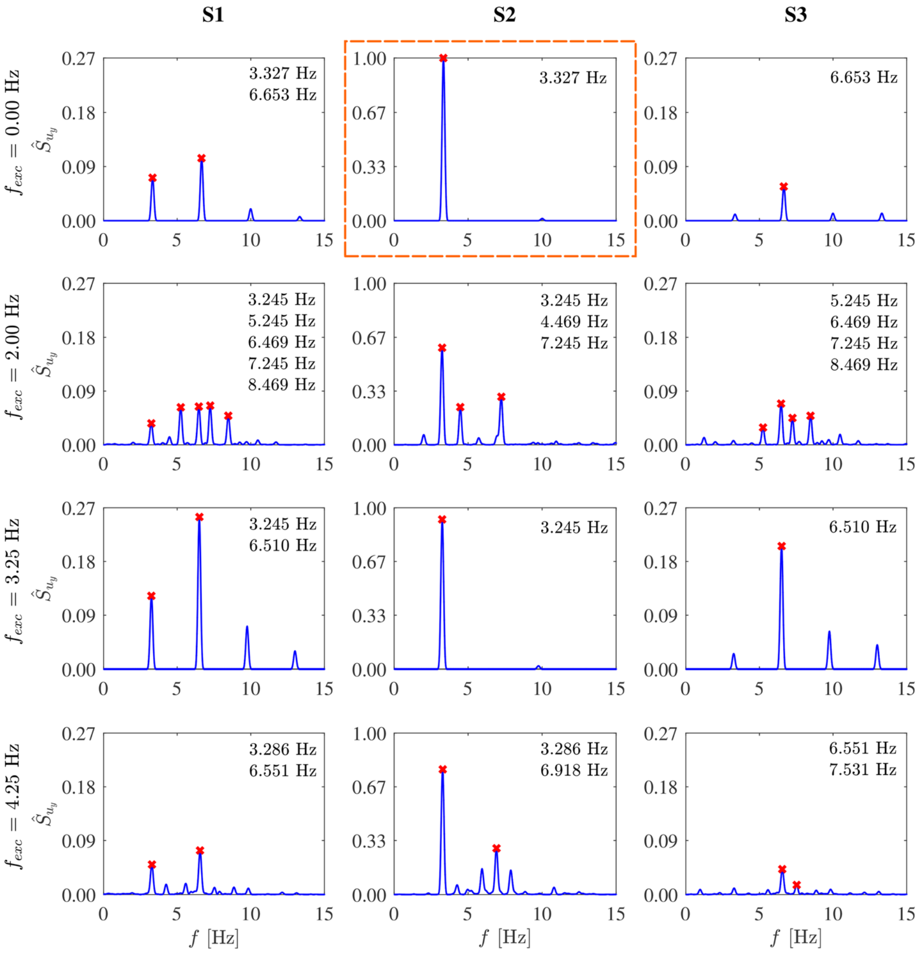

FIG. 9. The normalized PSDs of the velocity component u_y at the probe points S1, S2, and S3 (from left to right) at various f_{exc}. The PSDs are normalized by the peak magnitude at 3.327 Hz of the PSD at S2 in the stationary case, which is encircled by the dashed box in orange. The predominant peaks are marked out with red cross symbols, and the corresponding frequencies are listed aside.

on the basis of the PSD peak magnitude of the stationary case, where only one peak is observed at $f_L = 3.327$ Hz (see Fig. 10). The first natural frequency of the splitter plate, $f_{n,1} = 3.236$ Hz from the FEM presented in Table III, is chosen as a reference to evaluate the resultant characteristic frequencies. Here $f_{L,M}$ denotes the frequency of the largest peak, and $f_{L,L}$ and $f_{L,R}$ are the frequencies of the secondary peaks below and above $f_{L,M}$, respectively. The criterion to choose the peaks is that peak magnitudes should be larger than 5% of the largest peak magnitude in a PSD spectrum. In other words, small peaks below the critical value are disregarded. In the lock-in regime, $f_{L,M}$ is equal to the enforced oscillation frequency f_{exc}. This suggests that the force generation is only controlled by the active pitch oscillation. Furthermore, the peak magnitudes in the lock-in regime are larger than those outside the regime. Especially, the largest magnitude is noticed at $f_{exc} = 3$ Hz, where the largest values of $C_{L,RMS}$, $C_{D,RMS}$, and $C_{D,mean}$ are also found (see Fig. 11).

However, for $f_{exc} = 2.75$, 3.625, and 3.75 Hz that are outside but next to the lock-in regime, the frequencies of the predominant structural response are still equal to f_{exc}. There are two different effects at these frequencies in comparison with the lock-in. First, a secondary peak frequency $f_{L,R}$ is seen for $f_{exc} = 2.75$ Hz, while $f_{L,L}$ for 3.75 Hz. The other effect is that the peak magnitudes are much smaller than those in the lock-in regime. Secondary frequencies are invisible for $f_{exc} = 3.625$ Hz, since the peaks (which are marked out with cyan circles for $\hat{S}_L$ in Fig. 10) are too small to consider based on the evaluation criterion given above. These secondary peak frequencies lead to the disordered trajectories, as observed in Figs. 4 and 5. Given these special effects, it is deemed that semi-lock-in regimes are formed around these enforced frequencies.

As illustrated in Fig. 12, another interesting phenomenon is that for f_{exc} outside the lock-in and semi-lock-in regimes (that is, in the non-lock-in regimes), $f_{L,M}$ is always identified around the first natural frequency of the splitter plate $f_{n,1}$. Moreover, secondary peak frequencies of both $f_{L,L}$ and $f_{L,R}$ are clearly visible. Even more interestingly, the secondary peak frequencies are distributed along the line defined by $f_L = f_{exc}$, as well as the two lines (colored in blue and red in the figure) following the ratio of $\Delta f_L / \Delta f_{exc} = -1$. Note that another ratio of $\Delta f_L / \Delta f_{exc} = 1$ is derived from $f_L = f_{exc}$. Thus, the flow field is influenced by the combined effects of the passive structural characteristics and the active pitch oscillation. The largest peak magnitude of $\hat{S}_L$ among all the cases is observed at $f_{exc} = 3$ Hz, but not at another enforced frequency that is more close to $f_{n,1}$. By looking at the lines highlighted in the figure, this enforced frequency is located at the intersection point of the lines following $f_L = f_{exc}$ and the -1 ratio.

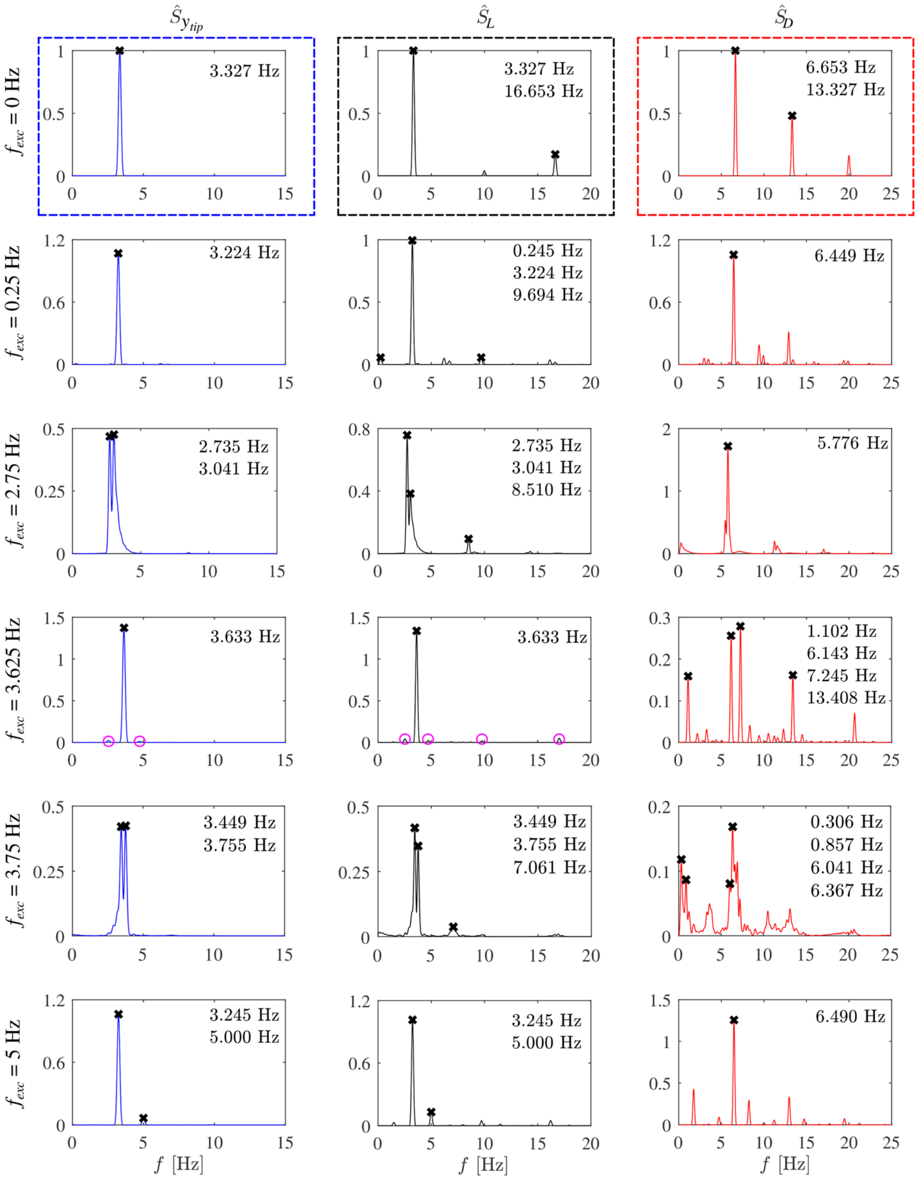

FIG. 10. The normalized PSDs of the tip displacement ($\hat{S}_{y_{tip}}$), the lift force ($\hat{S}_L$), and the drag force ($\hat{S}_D$) at different f_{exc}. The PSDs of each variable are normalized in reference to those at $f_{exc} = 0$ Hz, which are displayed within the dashed boxes. The cyan circles in the plots at $f_{exc} = 3.625$ Hz mark the peaks that have nearly negligible amplitudes.

D. Structural responses of the splitter plate

The values of f_{res} for the most predominant peaks in the normalized PSDs, $\hat{S}_{y_{tip}}$, are plotted with respect to f_{exc} in Fig. 13. The normalization is based on the magnitude of the dominant peak in the stationary case with $f_{exc} = 0$ Hz. Here $f_{res,M}$ denotes the frequency of the largest peak, and $f_{res,L}$ and $f_{res,R}$ are the frequencies of the second or third largest peaks below and above $f_{res,M}$, respectively. The criterion to choose the peaks is that peak magnitudes should be larger than 2% of the largest magnitude in the respective PSD spectrum. The symbols in the figure are colored with the PSD magnitudes. The first natural frequency, $f_{n,1} = 3.236$ Hz computed using the FEM (see Table III), is defined as a reference point for the evaluation. The FFT for computing the spectra of the splitter-plate tip displacements adopts the same signal processing parameters and setup as those used to do the spectral analysis for f_{res} in Table II.

As shown in Fig. 13, in the range of f_{exc} from 2.75 to 3.75 Hz, the values of f_{res} are aligned with the relationship of $f_{res,M} = f_{exc}$, namely, the ratio of $\Delta f_{res,M}/\Delta f_{exc} = 1$. This trend is also observed for the lift force PSDs in Fig. 12. The frequency range covers the lock-in and semi-lock-in regimes according to the analysis of the lift force PSDs. This suggests that the enforced pitch oscillation plays an important role in controlling the energy absorption of the structure. The oscillation dominates the resonant responses of the splitter-plate structure, which significantly interact with flow vortices. This specific lock-in effect due to the enforced pitch is different from classical lock-in effects found in the VIV of the benchmark stationary case at $f_{exc} = 0$ Hz[27,47]

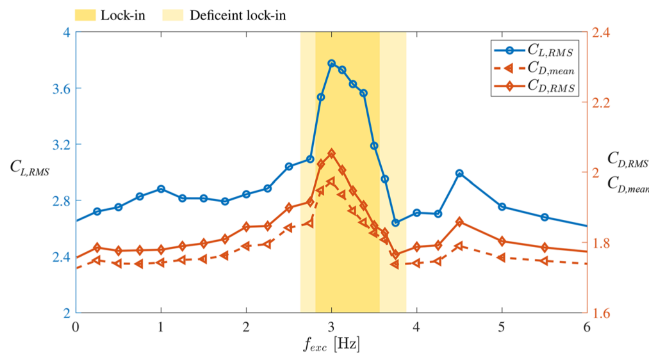

FIG. 11. The RMS lift coefficient, $C_{L,RMS}$, and the time-averaged and RMS drag coefficients, $C_{D,mean}$ and $C_{D,RMS}$, as a function of the enforced oscillation frequency f_{exc}.

or a stationary circular cylinder.[27,33] In these stationary blunt body scenarios where the free-stream velocity U_0 can be adapted within a wide range at low Reynolds numbers, the frequencies of the lock-in regime are found being dependent on the reduced velocity ratio that is defined as $U_0/(f_{n,1}D)$.

Like the frequency distribution of $\hat{S}_L$ (see Fig. 12), an interesting phenomenon for the non-lock-in regimes in Fig. 13 is that apart from the most dominant peak $f_{res,M} \approx f_{n,1}$, two secondary peaks $f_{res,L}$ and $f_{res,R}$ are identified in the non-lock-in frequencies of f_{exc} ranging from 1.5 to 2.5 and 4 to 4.25 Hz. These secondary peaks are distributed along three lines with the ratios of $\Delta f_{res}/\Delta f_{exc} = \pm 1$, where the ratio of 1 is derived from $f_{res} = f_{exc}$. Moreover, secondary peaks are not identified at comparatively lower and higher enforced frequencies of $f_{exc} \leq 1.25$ and ≥ 4.5 Hz. Therefore, the passive structural responses determined by the natural frequencies are mainly significant in the non-lock-in regimes, in particular at frequencies far from the lock-in regime. In contrast, in the lock-in and semi-lock-in regimes, the effects of the enforced pitch oscillation overwhelm the passive responses and furthermore determine the energy conversion from the flow to the structure deformation.

VI. DISCUSSIONS

To confirm the ratios of $\Delta f_{res}/\Delta f_{exc} = \pm 1$, Fig. 14 shows the absolute differences between the secondary peak frequencies ($f_{res,L}$ and $f_{res,R}$) and the predominant peak $f_{res,M}$ as a function of the enforced oscillation frequency f_{ext}. The left peak difference is calculated as $\Delta f_{res,L} = f_{res,M} - f_{res,L}$, and the right peak difference as $\Delta f_{res,R} = -f_{res,M} + f_{res,R}$. According to the analysis for Fig. 13, the secondary peak frequencies appear at f_{exc} from 1.5 to 2.5 and 4 to 4.25 Hz. Examples for the calculation at $f_{exc} = 2.25$ and 4 Hz are illustrated in Fig. 14. As can be seen in this figure, $\Delta f_{res,L}$ and $\Delta f_{res,R}$ are nearly equal to each other at every enforced frequency of interest. In other words, the two secondary peak frequencies, $f_{res,L}$ and $f_{res,R}$, are nearly symmetric with respect to the frequency of the largest peak $f_{res,M}$, resulting in the ratios of ± 1. The same effects have also been observed for the lift force PSDs $\hat{S}_L$, while the data are not plotted here for the sake of brevity.

Comparing all the cases in terms of the magnitudes of the most predominant peaks in the lift force PSDs (see Fig. 12) and the tip displacement PSDs (see Fig. 13), the smallest values are found at $f_{exc} = 2.75$ and 3.75 Hz outside the lock-in regime. The cases with these two enforced frequencies as well as 3.625 Hz exhibit that $f_{L,M}$ and $f_{res,M}$ are dependent on f_{exc} like those in the lock-in regime. On the other hand, as indicated in Figs. 4–6, the trajectories of the tip displacement, lift, and drag become disordered at these enforced frequencies. This is because a secondary peak commences to play a role, which is identified in Fig. 10. Additionally, as found in Fig. 11, the force coefficients of $C_{L,RMS}$, $C_{D,mean}$, and $C_{D,RMS}$ alter obviously at these enforced frequencies. By synthetically considering all of these effects, $f_{exc} = 2.75$, 3.625, and 3.75 Hz are, therefore, deemed to be in semi-lock-in regimes, which exist next to the lock-in regime.

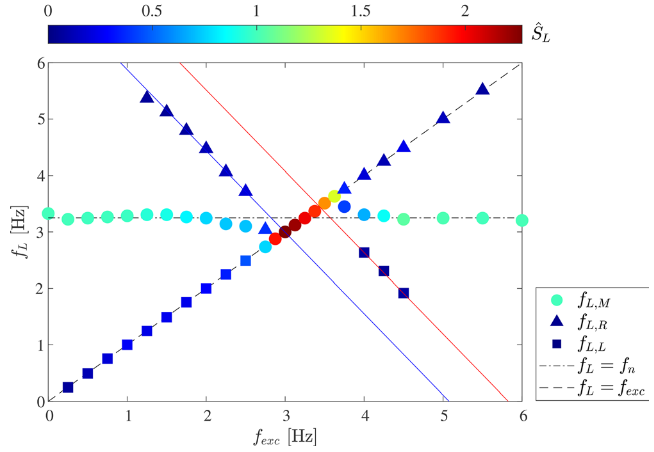

FIG. 12. The maximum peak frequency in the PSDs of the lift force, $f_{L,M}$, and the secondary peak frequencies, $f_{L,L}$ and $f_{L,R}$, with respect to f_{exc}. The symbols are colored with the normalized magnitudes of the PSDs, $\hat{S}_L$, at these frequencies. The dash-dotted line marks out the natural frequency of the splitter plate of $f_{n,1} = 3.236$ Hz; the blue and red solid lines are drawn based on the ratio of $\Delta f_L/\Delta f_{exc} = -1$.

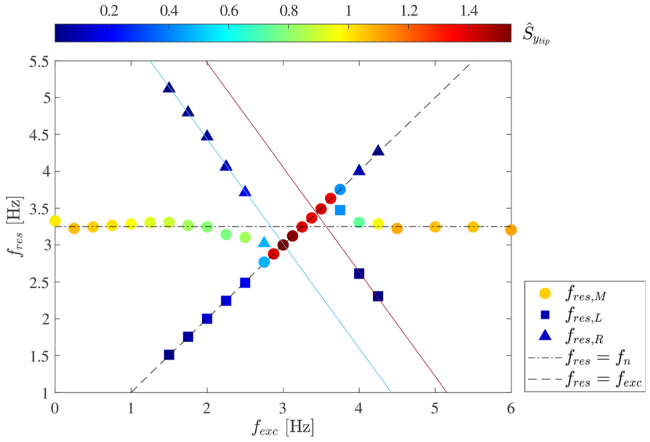

FIG. 13. The peak frequencies (i.e., the maximum peak frequency $f_{res,M}$, the secondary peak frequencies $f_{res,L}$ and $f_{res,R}$ below and above $f_{res,M}$) of the normalized splitter-plate tip displacement PSD $\hat{S}_{y_{tip}}$ with respect to f_{exc}. The symbols are colored with the normalized magnitudes of the PSDs, $\hat{S}_{y_{tip}}$, at these frequencies. The dash-dotted line indicates the natural frequency of the plate of $f_{n,1} = 3.236$ Hz; the blue and red solid lines are plotted based on the ratio of $\Delta f_{res}/\Delta f_{exc} = -1$.

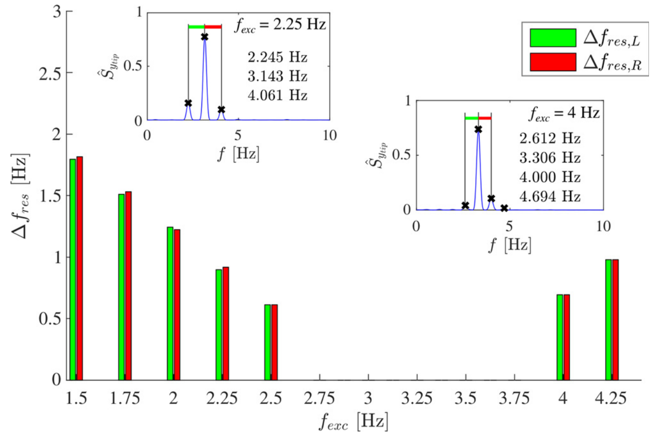

FIG. 14. The absolute differences between the secondary peak frequencies of the splitter-plate structural responses ($f_{res,L}$ and $f_{res,R}$) and the largest peak frequency $f_{res,M}$, as a function of the enforced oscillation frequency f_{exc}. These frequencies are referred to Fig. 13.

Considering the lines following the ratios of ±1 in Fig. 12 or 13, two intersection points of the lines are located at $f_{exc} = 3$ and 3.44 Hz. These frequencies are very closed to the frequency limits of the lock-in regime, which are 2.875 and 3.5 Hz. Thus, it is deduced that the onset of the lock-in effects is associated with the conditions at the intersection points. At $f_{exc} = 3$ Hz, the largest peak magnitude presents in both $\hat{S}_L$ and $\hat{S}_{y_{tip}}$. The peak magnitudes in the semi-lock-in regimes in both PSDs are smaller than those in the lock-in and non-lock-in regimes.

For the lift force and tip displacement, the common relationships explored to determine the peak frequency distribution in the PSDs are summarized as follows. Here, either f_L or f_{res} is simply signified as f for brevity.

- If f_{exc} is in the lock-in regime,

$$f_M = f_{exc} \;\Rightarrow\; \Delta f_M/\Delta f_{exc} = 1. \tag{12}$$

- If f_{exc} is in the semi-lock-in regimes,

$$\begin{cases} f_M = f_{exc} \;\Rightarrow\; \Delta f_M/\Delta f_{exc} = 1 \\ f_R \in (f_M, f_{n,1}) \;\; \& \text{ invisible } \;\; f_L, \quad \text{for} \quad f_{exc} < f_{cr,min} \\ f_L \in (f_{n,1}, f_M) \;\; \& \text{ invisible } \;\; f_R, \quad \text{for} \quad f_{exc} > f_{cr,max}. \end{cases} \tag{13}$$

  Here $f_{cr,min}$ and $f_{cr,max}$ are the minimum and maximum critical values of the enforced frequency for the lock-in regime, respectively. In the current study, $f_{cr,min}$ is around 2.875 Hz, and $f_{cr,max}$ is around 3.5 Hz. Note that for $f_{exc} = 3.625$ Hz, f_L is also invisible because of the negligible spectral magnitude at this frequency (see Fig. 10).

- If f_{exc} is outside the lock-in regime,

$$\begin{cases} f_M \approx f_{n,1} \\ f_i = f_{exc} \;\Rightarrow\; \Delta f_i/\Delta f_{exc} = 1, \quad i = L \, or \, R \\ \Delta f_i/\Delta f_{exc} = -1. \end{cases} \tag{14}$$

VII. CONCLUSIONS

The combination of the passive VIV and active pitch oscillation is investigated for a square cylinder assembled with a flexible splitter plate at a low Reynolds number of 333. The enforced oscillation frequency, f_{exc}, ranges from 0 to 6 Hz, and the oscillation amplitude is kept as a constant of 3°. The stationary-cylinder case for this configuration with $f_{exc} = 0$ Hz has been widely investigated as a benchmark VIV case. This facilitates the validation of the method used in this study and furthermore the understanding of how the actively enforced pitch oscillation affects the VIV in reference to the stationary-cylinder case.

The trajectories of the lift and drag coefficients evolving in time are disordered, except for the stationary case and those with f_{exc} between 2.875 and 3.5 Hz where the trajectories are in simple closed loops. Even though a very low frequency of 0.25 Hz is enforced, the lift and drag are affected. The area within which a disordered trajectory varies is dependent on f_{exc}. Likewise, the trajectories of the splitter-plate tip displacement with respect to either lift or drag exhibit similar behaviors. Based on the trajectory patterns, a lock-in regime of $f_{exc} \in [2.875, 3.75]$ Hz is deduced, since the simple closed loops indicate the lock-in interaction between the flow and the splitter plate. The zero lift and the smallest drag in the lock-in regime are achieved on most occasions when the tip of the splitter plate is at non-neutral position, while an exception is at 2.875 Hz where the lift is not zero.

The RMS values of the lift coefficient and the RMS and time-averaged values of the drag coefficient show similar trends in the dependence on f_{exc}. A remarkable change of these values is found in the lock-in regime. The coefficients become the largest at 3 Hz, which implies the most significant lock-in interaction being excited, despite that the first natural frequency of the splitter plate is $f_{n,1} = 3.236$ Hz.

For the cases with $f_{exc} = 2.75$, 3.625, and 3.75 Hz, the flow and structural vibrations show special features mixing lock-in and non-lock-in effects. As in the lock-in regime, the frequencies of the largest peaks in the PSDs of the lift force and tip displacement are nearly equal to the corresponding f_{exc}. However, the magnitudes of the largest peaks are smaller than in all other cases. Since a secondary peak frequency onsets, the trajectories of the tip displacement with respect to the lift and drag forces become disordered, as in the non-lock-in regime. The time-averaged and RMS values of the force coefficients also alter significantly. Therefore, the regimes encompassing these enforced frequencies are deemed as semi-lock-in regimes.

By extracting the predominant peak frequencies f_L from the PSDs of the lift force, it is found that these frequencies are distributed by following three characteristic relationships such as $f_L \approx f_{n,1}$, $f_L = f_{exc}$ (i.e., $\Delta f_L/\Delta f_{exc} = 1$), and $\Delta f_L/\Delta f_{exc} = -1$. In the lock-in regime, only one predominant peak at $f_{L,M}$ presents in every case, and it satisfies $f_{L,M} = f_{exc}$. This relationship is also found in the semi-lock-in regimes, while additionally a secondary peak appears at a frequency between $f_{L,M}$ and $f_{n,1}$. In the non-lock-in regimes, $f_{L,M} \approx f_{n,1}$; and the frequencies of the two secondary predominant peaks, $f_{L,L}$ and $f_{L,R}$, are distributed to follow $f_L = f_{exc}$ and the ratio of $\Delta f_L/\Delta f_{exc} = -1$. Moreover, the characteristic lines intersect with each other at $f_{exc} = 3$ and 3.44 Hz, which are very close to the frequency limits of the lock-in regime. The largest peak magnitude among all the cases presents at $f_{exc} = 3$ Hz. These results suggest that the onset of the lock-in effects is triggered by the conditions at the intersection points.

The tip displacement exhibits the same spectral characteristics as those found for the lift force. The characteristic relationships addressed for the lift force and tip displacement infer that the interaction between the flow and current configuration is dependent on the combined effects of the passive VIV and actively enforced pitch oscillation. On the other hand, in the specific lock-in regime caused by adjusting f_{exc}, only the enforced pitch oscillation dominates the interaction.

Nonetheless, the present study has not analyzed the parameters, such as the pitch magnitude, the center of rotation, the length of the splitter plate, and Reynolds numbers. Their effects are interesting to address in future work. Furthermore, when high Reynolds numbers are concerned, more complex simulations with turbulence modeling techniques will be requested to solve relevant issues. It is also worth noting that secondary instability onsets at the Reynolds number in this study. Flow simulation in 3D is of interest to understand spanwise mechanisms, which are neglected in the present 2D simulations.

It is interesting to extend the present study of the square cylinder to a circular cylinder, such as the Turek–Hron benchmark.[18] As both blunt bodies induce vortex streets, it is anticipated that similar results might be achieved in a circular cylinder case. On the other hand, galloping exists for a square cylinder, but not for a circular cylinder, at low Reynolds numbers.[48,49] Extensive numerical or experimental research in the future should be carried out to confirm these anticipations.

ACKNOWLEDGMENTS

We thank Dr. Rameez Badhurshah and Dr. Massoud Tatar for discussions on VIV. This work received funding from the Swedish Transport Administration in the project GEMINI (GEneric Multidisciplinary optimization for sail INstallation on wInd-assisted ships GEMINI) and from Chalmers University of Technology Foundation in the strategic research project "Hydro- and Aerodynamics." The computations and data handling were enabled by resources provided by the Swedish National Infrastructure for Computing (SNIC), partially funded by the Swedish Research Council through Grant Agreement No. 2018-05973.

AUTHOR DECLARATIONS

Conflict of Interest

The authors have no conflicts to disclose.

Author Contributions

Aravindhan Venkatesh: Formal analysis (equal); Investigation (equal); Methodology (equal); Validation (equal); Visualization (equal); Writing – original draft (equal). **Jiqiang Niu:** Formal analysis (equal); Funding acquisition (equal); Methodology (equal); Software (equal); Supervision (equal); Writing – review & editing (equal). **Xiao Xue:** Data curation (equal); Validation (equal); Visualization (equal). **Zheng-Wei Chen:** Data curation (equal); Validation (equal); Visualization (equal). **Hua-Dong Yao:** Conceptualization (equal); Data curation (equal); Formal analysis (equal); Funding acquisition (equal); Investigation (equal); Methodology (equal); Project administration (equal); Resources (equal); Software (equal); Supervision (equal); Validation (equal); Visualization (equal); Writing – original draft (equal); Writing – review & editing (equal).

DATA AVAILABILITY

The data that support the findings of this study are available within the article.

REFERENCES

[1] Y. Yu, Y. Liu, and X. Amandolese, "A review on fluid-induced flag vibrations," Appl. Mech. Rev. **71**, 010801 (2019).

[2] S. Nilsson, H.-D. Yao, A. Karlsson, and S. Arvidson, "Effects of viscosity and density on the aeroelasticity of the ONERA M6 wing from subsonic to supersonic speeds," in *AIAA Aviation 2022 Forum* (AIAA, 2022).

[3] W. A. Wall, "Fluid-struktur-interaktion mit stabilisierten finiten elementen," Ph.D. thesis (University of Stuttgart, 1999).

[4] H. G. Matthies and J. Steindorf, "Partitioned strong coupling algorithms for fluid-structure interaction," Comput. Struct. **81**(8–11), 805–812 (2003).

[5] W. Dettmer and D. Perić, "A computational framework for fluid-structure interaction: Finite element formulation and applications," Comput. Methods Appl. Mech. Eng. **195**(41–43), 5754–5779 (2006).

[6] M. Olivier, J.-F. Morissette, and G. Dumas, "A fluid-structure interaction solver for nano-air-vehicle flapping wings," in *19th AIAA Computational Fluid Dynamics* (AIAA, 2009).

[7] C. Wood, A. Gil, O. Hassan, and J. Bonet, "Partitioned block-Gauss-Seidel coupling for dynamic fluid-structure interaction," Comput. Struct. **88**(23–24), 1367–1382 (2010).

[8] C. Kassiotis, A. Ibrahimbegovic, R. Niekamp, and H. G. Matthies, "Nonlinear fluid–structure interaction problem. Part I: Implicit partitioned algorithm, nonlinear stability proof and validation examples," Comput. Mech. **47**, 305–323 (2011).

[9] C. Habchi, S. Russeil, D. Bougeard, J.-L. Harion, T. Lemenand, A. Ghanem, D. Della Valle, and H. Peerhossaini, "Partitioned solver for strongly coupled fluid-structure interaction," Comput. Fluids **71**, 306–319 (2013).

[10] H.-D. Yao, M. Y. Svensson, and H. Nilsson, "Deformation of dorsal root ganglion due to pressure transients of venous blood and cerebrospinal fluid in the cervical vertebral canal," J. Biomech. **76**, 16–26 (2018).

[11] B. Schott, C. Ager, and W. A. Wall, "A monolithic approach to fluid-structure interaction based on a hybrid Eulerian-ALE fluid domain decomposition involving cut elements," arXiv:1808.003431 (2018).

[12] E. M. Binyet, J.-Y. Chang, and C.-Y. Huang, "Flexible plate in the wake of a square cylinder for piezoelectric energy harvesting—Parametric study using fluid-structure interaction modeling," Energies **13**, 2645 (2020).

[13] E. Binyet, C.-Y. Huang, and J.-Y. Chang, "Water tunnel study of a cantilever flexible plate in the wake of a square cylinder," Microsyst. Technol. **26**, 3435–3449 (2020).

[14] M. Furquan and S. Mittal, "Flow past two square cylinders with flexible splitter plates," Comput. Mech. **55**, 1155–1166 (2015).

[15] M. Sarioglu, "Control of flow around a square cylinder at incidence by using a splitter plate," Flow Meas. Instrum. **53**, 221–229 (2017).

[16] S. Turki, "Numerical simulation of passive control on vortex shedding behind square cylinder using splitter plate," Eng. Appl. Comput. Fluid Mech. **2**(4), 514–524 (2008).

[17] M. S. M. Ali, C. J. Doolan, and V. Wheatley, "Low Reynolds number flow over a square cylinder with a splitter plate," Phys. Fluids **23**, 033602 (2011).

[18] S. Turek and J. Hron, "Proposal for numerical benchmarking of fluid-structure interaction between an elastic object and laminar incompressible flow," in *Fluid-Structure Interaction*, Lecture Notes in Computational Science and Engineering, Vol. 53, edited by H. Bungartz and M. Schäfer (Springer, 2006).

[19] N. F. Giannelis and G. A. Vio, "Computational benchmark of commercial fluid-structure interaction software for aeroelastic applications," in *International Forum on Aeroelasticity and Structural Dynamics (IFASD)* (IFASD, 2015).

[20] T. R. Sahu, M. Furquan, and S. Mittal, "Numerical study of flow-induced vibration of a circular cylinder with attached flexible splitter plate at low Re," J. Fluid Mech. **880**, 551–593 (2019).

[21] J.-L. Pfister and O. Marquet, "Fluid-structure stability analyses and nonlinear dynamics of flexible splitter plates interacting with a circular cylinder flow," J. Fluid Mech. **896**, 24 (2020).

[22] M. Tatar and H.-D. Yao, "Flow field interference effect on energy harvesting enhancement of a combined fluid–structure interaction system in channel flow," Phys. Fluids **36**, 023606 (2024).

[23] F. Duan and J. Wang, "Fluid–structure–sound interaction in noise reduction of a circular cylinder with flexible splitter plate," J. Fluid Mech. **920**, 6 (2021).

[24] J. Lin and H.-D. Yao, "Modified Magnus effect and vortex modes of rotating cylinder due to interaction with free surface in two-phase flow," Phys. Fluids **35**, 123614 (2023).

[25] S. Kasmaiee, M. Tadjfar, and S. Kasmaiee, "Machine learning-based optimization of a pitching airfoil performance in dynamic stall conditions using a suction controller," Phys. Fluids **35**, 095121 (2023).

[26] S. Kasmaiee, M. Tadjfar, and S. Kasmaiee, "Optimization of blowing jet performance on wind turbine airfoil under dynamic stall conditions using active machine learning and computational intelligence," Arab. J. Sci. Eng. **49**, 1771–1795 (2024).

[27] A. Kundu, A. K. Soti, H. Garg, R. Bhardwaj, and M. C. Thompson, "Computational modeling and analysis of flow-induced vibration of an elastic splitter plate using a sharp-interface immersed boundary method," SN Appl. Sci. **2**, 1110 (2020).

[28] B. Hübner, E. Walhorn, and D. Dinkler, "A monolithic approach to fluid–structure interaction using space–time finite elements," Comput. Methods Appl. Mech. Eng. **193**, 2087–2104 (2004).

[29] F. Boyer, G. D. Nayer, A. Leroyer, and M. Visonneau, "Geometrically exact Kirchhoff beam theory: Application to cable dynamics," J. Comput. Nonlinear Dyn. **6**(4), 041004 (2011).

[30] R. D. Henderson and D. Barkley, "Secondary instability in the wake of a circular cylinder," Phys. Fluids **8**, 1683–1685 (1996).

[31] C. H. K. Williamson, "Mode a secondary instability in wake transition," Phys. Fluids **8**, 1680–1682 (1996).

[32] T. R. Sahu, M. Furquan, Y. Jaiswal, and S. Mittal, "Flow-induced vibration of a circular cylinder with rigid splitter plate," J. Fluids Struct. **89**, 244–256 (2019).

[33] C. Mittal and A. Sharma, "Flow-induced vibration of a flexible splitter-plate in the wake of a stationary cylinder," Phys. Fluids **33**(11), 113607 (2021).

[34] S. Frei, B. Holm, T. Richter, T. Wick, and H. Yang, *Fluid-Structure Interaction: Modeling, Adaptive Discretisations and Solvers*, 1st ed. (Walter de Gruyter GmbH, Berlin/Boston, 2017).

[35] C. W. Hirt, A. A. Amsden, and J. Cook, "An arbitrary Lagrangian-Eulerian computing method for all flow speeds," J. Comput. Phys. **14**, 227–253 (1974).

[36] C. Farhat, P. Geuzaine, and C. Grandmont, "The discrete geometric conservation law and the nonlinear stability of ALE schemes for the solution of flow problems on moving grids," J. Comput. Phys. **174**(2), 669–694 (2001).

[37] M. A. Fernández, J.-F. Gerbeau, and C. Grandmont, "A projection semi-implicit scheme for the coupling of an elastic structure with an incompressible fluid," Numer. Meth. Eng. **69**, 794–821 (2007).

[38] A. Quaini and A. Quarteroni, "A semi-implicit approach for fluid-structure interaction based on an algebraic fractional step method," Math. Models Methods Appl. Sci. **17**(6), 957–983 (2007).

[39] A. de Boer, A. H. van Zuijlen, and H. Bijl, "Comparison of conservative and consistent approaches for the coupling of non-matching meshes," Comput. Methods Appl. Mech. Eng. **197**(49), 4284–4297 (2008).

[40] S. V. Patankar and D. B. Spalding, "A calculation procedure for heat, mass and momentum transfer in three-dimensional parabolic flows," Int. J. Heat Mass Transfer **15**(10), 1787–1806 (1972).

[41] O. C. Zienkiewicz, R. L. Taylor, and J. Z. Zhu, *The Finite Element Method: Its Basis and Fundamentals*, 7th ed. (Elsevier Butterworth-Heinemann, Oxford, 2013).

[42] B. A. Finlayson, *The Method of Weighted Residuals and Variational Principles*, 1st ed. (Academic Press, New York, 1972).

[43] A. H. Stroud and D. Secrest, *Gaussian Quadrature Formulas* (Prentice-Hall, Englewood Cliffs, NJ, 1966).

[44] E. Ramm and W. Wall, "Fluid-structure interaction based upon a stabilized (ALE) finite element method," in *4th World Congress on Computational Mechanics: New Trends and Applications* (CIMNE, Barcelona, 1998), pp. 1–20.

[45] Y. Bazilevs, V. M. Calo, T. J. Hughes, and Y. Zhang, "Isogeometric fluid-structure interaction: Theory, algorithms, and computations," Comput. Mech. **43**(1), 3–37 (2008).

[46] S. S. Rao, *Vibration of Continuous Systems* (John Wiley & Sons, 2019).

[47] D. Kumar and S. Sen, "Flow-induced vibrations of a pair of in-line square cylinders," Phys. Fluids **33**, 043602 (2021).

[48] P. Han and E. de Langre, "There is no critical mass ratio for galloping of a square cylinder under flow," J. Fluid Mech. **9351**, 27 (2021).

[49] A. Joly, S. Etienne, and D. Pelletier, "Galloping of square cylinders in cross-flow at low Reynolds numbers," J. Fluids Struct. **28**, 232–243 (2012).